Rock Mech Rock Eng (2015) 48:2077–2091
DOI 10.1007/s00603-014-0693-7

ORIGINAL PAPER

New Soft Rock Pillar Strength Formula Derived Through Parametric FEA Using a Critical State Plasticity Model

Giuseppe Rastiello · Francesco Federico · Silvio Screpanti

Received: 20 July 2014 / Accepted: 29 November 2014 / Published online: 10 December 2014

Abstract Many abandoned room and pillar mines have been excavated not far from the surface of large areas of important European cities. In Rome, these excavations took place at shallow depths (3–15 m below the ground surface) in weak pyroclastic soft rocks. Many of these cavities have collapsed; others appear to be in a stable condition, although an appreciable percentage of their structural components (pillars, roofs, etc.) have shown increasing signs of distress from both the morphological and mechanical points of view. In this study, the stress–strain behaviour of soft rock pillars sustaining systems of cavities under vertical loads was numerically simulated, starting from the in situ initial conditions due to excavation of the cavities. The mechanical behaviour of the constituent material of the pillar was modelled according to the Modified Cam-Clay constitutive law (elasto-plastic with strain hardening). The influence of the pillar geometry (cross-section area, shape, and height) and mechanical parameters of the soft rock on the ultimate compressive strength of the pillar as a whole was parametrically investigated first. Based on the numerical results, an original relationship for pillar strength assessment was developed. Finally, the estimated pillar strengths according to the proposed formula and well-known formulations in the literature were compared.

G. Rastiello (✉)
LMT (ENS Cachan, CNRS, Université Paris Saclay), 61 Avenue du Président Wilson, 94235 Cachan Cedex, France
e-mail: g.rastiello@gmail.com; rastiello@lmt.ens-cachan.fr

F. Federico S. Screpanti
Department of Civil Engineering and Computer Science, University of Rome "Tor Vergata", Via del Politecnico 1, 00133 Rome, Italy

Keywords Room and pillar mines · Shallow cavities · Pillar strength · Soft rocks · Roman pozzolana · Numerical parametric study · Analytical relationship

List of symbols

χ	Pillar safety factor
σ_r	Pillar compressive strength
σ_p	Average pillar stress
σ_p^{γ}	Average pillar stress contribution due to the weight of coating soils
σ_p^{y}	Pillar yield stress on the $(\sigma_p, \varepsilon_p)$ curve
ε_p	Average pillar strain
ε_p^{y}	Average pillar strain at yielding
δv_{gs}	Imposed vertical ground surface displacements
A	Pillar cross-section area
b	Small side of pillar cross-section
l	Large side of pillar cross-section
d	Pillar diameter
h	Pillar height
b_{eq}	Side of equivalent square section pillar
b/h	Pillar width-to-height ratio
b_{eq}/h	Pillar average width-to-height ratio
σ_1	Material uniaxial compressive strength
σ_u	Unconfined compressive strength of a cubical pillar specimen
k_{lp}	Pillar shape term (Lunder and Pakalnis's formulation)
c_{pav}	Pillar average confinement (Lunder and Pakalnis's formulation)
p	Equivalent pressure
q	Deviator stress
$f(p,q)$	Yield function
$g(p,q)$	Plastic potential
$\varepsilon_{ij}^{pl(el)}$	Plastic (elastic) strain tensor

$\varepsilon_{\text{mag}}^{pl}$	Plastic strain magnitude
$\varepsilon_p^{\text{pl(el)}}$	Plastic (elastic) volumetric strain
$\varepsilon_q^{\text{pl(el)}}$	Plastic (elastic) deviator strain
p_c^*	Current size of the yield surface
J^{pl}	Plastic volume change
p_c	Preconsolidation pressure
M	Slope of the critical state line on the (p, q)-plane
λ	Logarithmic hardening constant in pure compression
k	Logarithmic bulk modulus in pure compression
E	Young's modulus
ϕ	Shear angle
c	Cohesion
v	Poisson's ratio
G	Elastic shear modulus
e	Void ratio
V	Specific volume

1 Introduction

Systems of abandoned room and pillar mines have been found in several European cities at shallow depths. The need for large amounts of building materials has historically led to the digging of extended underground mines, especially in areas bordering the oldest and most extended European cities (Rome, Naples, Paris, London, Maastricht, etc.), which today belong to the urban fabric. At present, these mines are tourist attractions or have been converted to other uses, such as growing of mushrooms.

In Rome, these cavities (rooms) have usually been excavated at shallow depths ($3 \div 15$ m from the ground surface) in weakly cemented pozzolana (pillars), under a layer of consistent tuffs (roofs or vaults). These rooms compose approximately regular grids, at one or more levels; the pillars are generally quadrangular in shape (Fig. 1). Multiple pillar failures and vault collapses are recurrent (Federico and Screpanti 2002, 2003b), which often lead to subsidence and localised depressions (i.e. sink-holes).

In room and pillar mines, pillars sustain the weight of coating soils and the overcharges applied on the ground surface. Their stability is often threatened by the mining operation itself (e.g. robbing on retreat) and the progressive degradation of soil properties. As a consequence, the pillar strength is reduced to a limit value, at which point some pillars could no longer support the overburden stress. Under this condition, the ratio χ of the pillar strength σ_r to the average vertical stress σ_p, acting on the pillar due to its own weight and the external loads, becomes equal to unity:

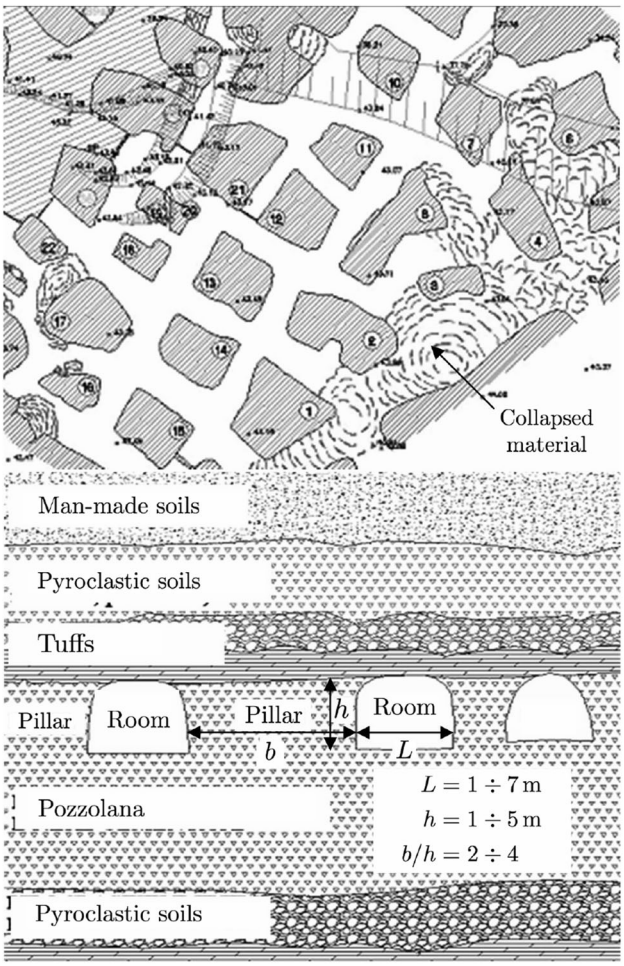

Fig. 1 Typical geometry of geotechnical system: representative plan of system of shallow cavities found in Roman subsoil

$$\chi = \frac{\sigma_r}{\sigma_p} = 1. \tag{1}$$

In general, assessing the stability of abandoned mines is very complex (Federico and Screpanti 2002). The failure of a single pillar induces a load transfer to adjacent pillars, which can cause them to fail too. Sometimes, a *domino*-type failure mechanism occurs (Martin and Maybee 2000). However, the interaction between adjacent pillars is extremely difficult to analyse, as plano-altimetric irregularity and material inhomogeneities should be considered. Therefore, pillars are usually considered as isolated and the working average stress σ_p is computed according to the so-called *tributary area method* (Bieniawski 1984; Brady and Brown 2004).

The pillar strength σ_r is estimated by means of empirical and semi-empirical formulas (Martin and Maybee 2000; Brady and Brown 2004). More advanced techniques are based on probabilistic approaches (Griffiths et al. 2002), analytical solutions (Qin et al. 2006; Wang et al. 2006) and

numerical methods (Murali Mohan et al. 2001; Mortazavi et al. 2009; Jaiswal and Shrivastva 2009).

Mainly developed in the context of mining engineering of hard rocks, conventional pillar strength formulas (Table 1) take the form of either power (Salamon and Munro 1967; Hedley and Grant 1972) or linear-type equations (Obert and Duvall 1967; Lunder and Pakalnis 1997). They may be summarised in the following unified mathematical form:

$$\sigma_r = \sigma_c \left(\alpha + \beta \frac{b^n}{h^m} \right) \quad (2)$$

where α, β, $n > 0$ and $m > 0$ are dimensionless parameters, b is the length of the small side of the pillar cross-section, h is the pillar height and σ_c is a measure of the compressive strength of the pillar material. Some useful summaries on pillar performances and strength formulas have been provided, among others, by Bieniawski (1984), Brady and Brown (2004) and González-Nicieza et al. (2006).

Because of the complex mechanical behaviour of soft rocks, such conventional approaches cannot be directly applied to pillars in pyroclastic materials. Therefore, their validation and adaptation to soft rock pillars play a key role in the development of proper procedures to estimate the safety conditions of abandoned urban mines.

To the best of the authors' knowledge, little experimental/numerical research on this topic is available in the literature. Therefore, in this study, finite element analyses (FEA) were performed to evaluate the resistance (compressive crushing) of soft rock pillars sustaining cavity systems. Pillar failure conditions were numerically simulated through increases in the vertical displacements of the ground surface, up to pillar collapse (Murali Mohan et al. 2001; Federico et al. 2010).

The behaviour of the soft rock was modelled according to an elastic–plastic strain-hardening constitutive law, specifically the Modified Cam-Clay model (Roscoe and Burland 1968; Schofield and Wroth 1968).

Based on the main features of the corresponding analytical formulations, the effect of the pillar geometry (area and shape of the horizontal cross-section, height) on the compressive strength σ_r, and the role of mechanical parameters of the constitutive law used to model the behaviour of the pillar material were investigated.

Based on a proper reorganisation of the numerical results, an original formula for estimating the strength of soft rock pillars was developed.

Table 1 Some conventional formulations to assess the compressive strength of hard rock pillars (σ_1 = material uniaxial compressive strength; σ_u = unconfined compressive strength of a cubical pillar specimen)

References	Formula	Unit
Bieniawski (1984)	$\sigma_r = \sigma_u \left(0.64 + 0.36 \frac{b}{h}\right)$	MPa
Obert and Duvall (1967)	$\sigma_r = \sigma_1 \left(0.778 + 0.222 \frac{b}{h}\right)$	MPa
Salamon and Munro (1967)	$\sigma_r = \sigma_u \frac{b^{0.46}}{h^{0.66}}$	MPa
Hedley and Grant (1972)	$\sigma_r = \sigma_1 \left(0.578 \frac{b^{0.5}}{h^{0.75}}\right)$	MPa
Von Kimmelmann et al. (1984)	$\sigma_r = \sigma_1 \left(0.691 \frac{b^{0.64}}{h^{0.66}}\right)$	MPa
Lunder and Pakalnis (1997)	$\sigma_r = 0.440\, \sigma_u \left(0.68 + 0.52 k_{lp}\right)$ where $k_{lp} = \tan\left(\cos^{-1}\left(\frac{1-c_{pav}}{1+c_{pav}}\right)\right)$ and $c_{pav} = 0.46\left(\log\left(\frac{b}{h} + 0.7\right)^{\frac{1.4}{b/h}}\right)$	MPa

2 Simplified Modelling of Soft Rocks Using the Modified Cam-Clay Model

Structured soils and soft rocks constitute a wide class of materials deriving from different geological processes (e.g. cementation, ageing and over-consolidation) and/or the progressive degradation of intact rocks due to weathering and/or temperature effects.

Because of intergranular bonds, their mechanical response is strongly dependent on the confining stress (Cecconi 1999). Under small confining pressures, the material behaviour is brittle-dilatant (i.e. rock-like); the stress–strain relationship is almost linear until a peak, which corresponds to the breaking of interparticle bonds (Airey 1993). In this phase, compressibility curves may exceed the normal compression line of the corresponding destructured material (Leroueil and Vaughan 1990); this condition is attained after yielding and is due to progressive degradation of interparticle bonds and granular crushing (Airey 1993; Coop and Atkinson 1993). At higher levels of confinement pressure, their behaviour becomes ductile-contractant (i.e. soil-like). In some cases, it is possible to identify a range of confinement pressures in which a brittle response with a marked peak corresponds to a contractant response (Lagioia and Nova 1996; Aversa and Evangelista 1998). Furthermore, if the response is dilatant, the condition of maximum rate of dilation does not correspond to the peak strength (Elliott and Brown 1985; Maccarini 1987).

Although the modified Cam-Clay (MCC) model (Roscoe and Burland 1968; Schofield and Wroth 1968) is not able to predict all of these aspects, its ability to represent the progressive transition from a brittle-dilatant response to a ductile-contractant response as the confining stress increases gives it the potential to represent soft rock behaviour. The main limitations are associated with the impossibility of representing some features proper to soft

rocks and, in general, to structured soils: (1) the tensile material strength is neglected; (2) the peak in the stress ratio (Rowe 1962) is always attained at the maximum dilatancy, and no peak stress ratio can be predicted for contractant regime (Elliott and Brown 1985; Cecconi et al. 2002; Coop and Atkinson 1993; Rouainia et al. 2000; (3) the change in slope of the compressibility curve in one-dimensional and isotropic compression, due to progressive material degradation, is not taken into account.

To overcome these limitations, many authors have introduced minor improvements to the original mathematical formulation, to account for cementation effects and thermo-hygro-chemo-mechanical degradation processes associated with grain collapse (Cecconi et al. 2002; DeSimone and Tamagnini 2005), de-bonding and weathering (Nova and Wood 1979; Nova et al. 2003).

However, the safe application of such advanced models for engineering purposes may reveal rather complex, with the main concern being parameter identification. For this reason, the MCC constitutive model was applied in the present study.

In the implementation of the model through the Abaqus FEA software (Simulia 2009), the material response in the plastic regime is defined by:

- a yield function $f(p,q)$, which depends on the equivalent pressure p and deviator stress q:

$$f(p,q) = \left(\frac{2p}{p_c^*} - 1\right)^2 + \left(\frac{2q}{Mp_c^*}\right)^2 - 1 = 0, \tag{3}$$

  where M is the slope of the critical state line in the (p,q)-space, and p_c^* defines the current size of the yield surface (i.e. the diameter of the yield locus on the (p,q)-plane);
- an associated flow rule $g(p,q) = f(p,q)$, which defines the plastic volumetric $d\varepsilon_p^{pl}$ and shear $d\varepsilon_q^{pl}$ strain rates:

$$d\varepsilon_p^{pl} = \frac{\partial g(p,q)}{\partial p} dp \quad d\varepsilon_q^{pl} = \frac{\partial g(p,q)}{\partial q} dq; \tag{4}$$

- an exponential strain-hardening law, which modifies the size of the yield locus according to the plastic volume change J^{pl}:

$$p_c^*(J^{pl}) = p_c \exp\left[(1+e_0)\frac{1-J^{pl}}{\lambda - kJ^{pl}}\right], \tag{5}$$

  where p_c is the initial size of the yield surface, e_0 is the initial void ratio, k is the logarithmic bulk modulus and λ is the logarithmic hardening constant for the elasto-plastic response in pure compression.

In the elastic regime, any recoverable change in the volumetric/shear strain is assumed to correspond to mean/deviator stress variations according to the following incremental relations:

$$d\varepsilon_p^e = -k\frac{dp}{Vp} \quad d\varepsilon_q^e = \frac{dq}{3G} \tag{6}$$

where V is the specific volume and G denotes the elastic shear modulus, computed using k and the Poisson's ratio ν.

Wood et al. (1992), Navarro et al. (2007) and Simulia (2009) presented some useful instructions concerning the identification of soil parameters for use with the MCC model. In general, at least two conventional experiments are required: an isotropic compression test to calibrate the values of p_c, λ and k; a triaxial test to calibrate the value of M.

The present study considered the set of parameters (λ, k, ν, M, p_c) identified by Federico and Screpanti (2003a) through an inverse analysis approach based on FEA simulated tests and experimental data for black Roman pozzolana (Cecconi 1999). For the stability analysis of abandoned mines, however, note that the model parameter identification carried out at the material scale is not sufficient (i.e. it only obtains the first estimate). The spatial variability of the mechanical properties of the involved materials, and the influence of their unknown history of loading call for a proper case-by-case parameter calibration. This, in turn, should be carried out through an inverse analysis approach based on the in situ analysis of some unstable/stable pillars.

For this reason, in the present research, the pillar stability conditions were numerically analysed through a parametric modelling approach. Finite element analyses were repeatedly performed considering the typical ranges of variation in the model parameters.

3 Numerical Simulation of Pillar Response

The mechanical response of a geotechnical system comprising coating soils, a vault, a pillar and its base (vertically loaded) was numerically analysed. Isolated pillars were schematically charged by the weight of overlying soil layers composing a tributary volume and the loads applied on the ground surface. According to this geometrical and mechanical modelling assumption, interactions between adjacent pillars and the loading history of each pillar were neglected. For the design of new mines, this may represent a quite strong simplification. However, in abandoned underground mines, pillars have often been mined for centuries; so, the realistic simulation of the pillar excavation phases and their loading history is extremely difficult.

Three-dimensional (3D) finite element (FE) models were developed by taking into account geometric, loading and material symmetries. Only one-quarter of the whole system beneath the tributary area was modelled. The roof of the cavity was 12 m below the ground surface and the base of the cavity parametrically varied between 15.5 and

17.5 m below the ground surface; consequently, the pillar heights ranged between 3.5 and 5.5 m. The total thickness of the model was limited to 30.5 m, as preliminary analyses had shown that, at grater depths, the increase in vertical stress induced by external loads was less than 5 % of the initial overburden pressure.

The simulated stratigraphy represents a typical stratigraphic sequence of the Roman area (see Fig. 2). The soil layers were assumed to be homogeneous, and the constituting materials were assumed to be isotropic with respect to the mechanical response. The relevant mechanical models and the corresponding characteristic parameters were chosen according to typical values of materials in the Roman area (Table 2).

Because of the strain-softening material behaviour, the numerical results could be non-objective with respect to the computational mesh (i.e. mesh-dependent). Thus, preliminary analyses were performed to evaluate the effect of the FE size on the stress–strain behaviour of the pillar and to estimate optimal meshes. For the representative model depicted in Fig. 2, the optimal mesh comprised approximately 250,000 linear hexaedrical finite elements (FEs). Their density increased near the pillar and roof, where high gradients of stresses and strains were expected.

Final FE models were obtained through a preliminary simulation of the excavation of rooms adjacent to the pillar. The simultaneous enlargement of the four galleries contouring the pillar was modelled through the progressive deactivation of groups (rows) of finite elements, starting from symmetry axes of the rooms and for their whole height. This modelling strategy allowed the description of

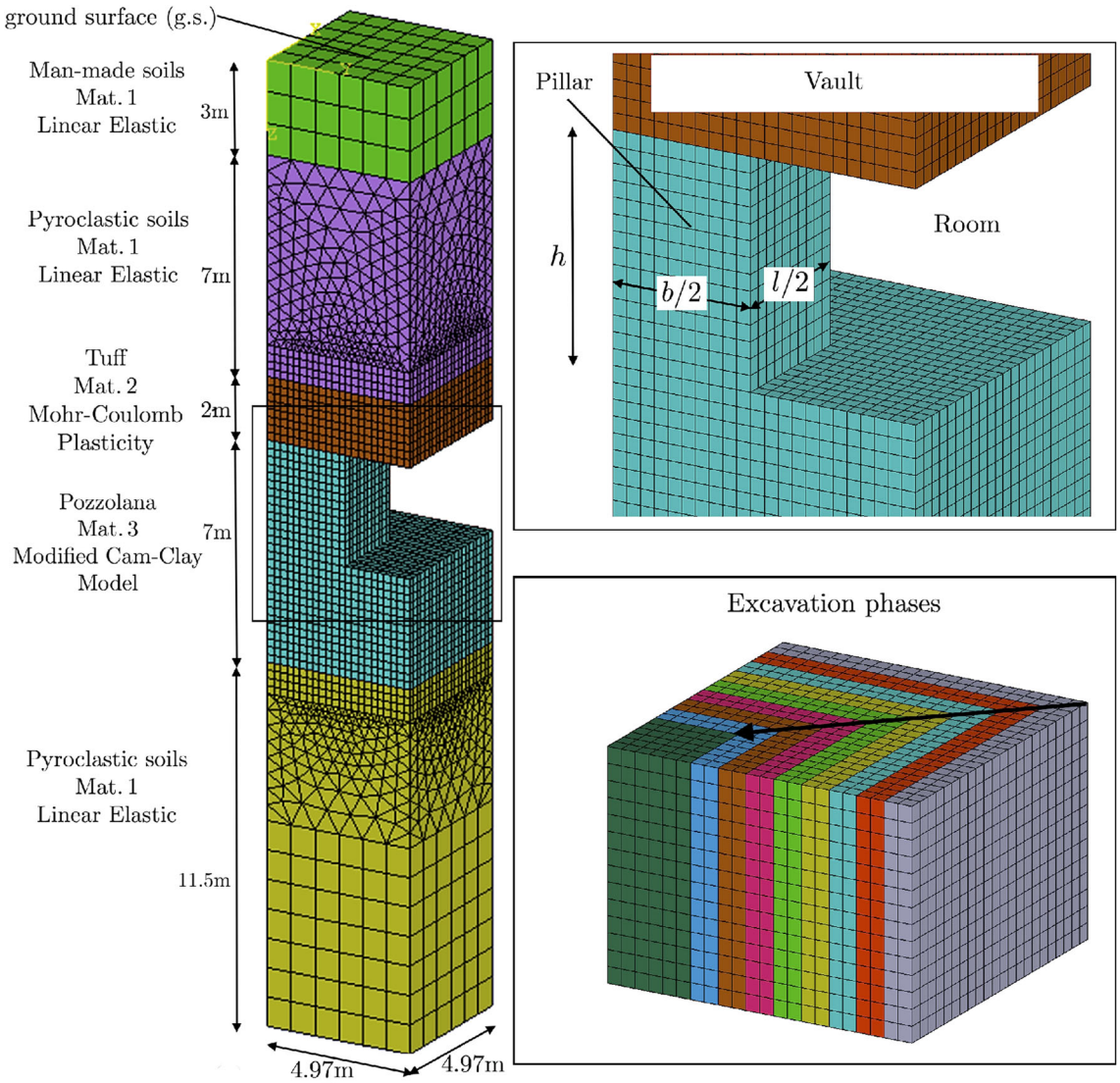

Fig. 2 Representative finite element model and definition of FE groups to be removed to simulate excavation for consecutive rows

Table 2 Physical and mechanical parameters characterising involved materials

Mat.	Model	E (MPa)	v	ϕ (°)	c (MPa)	λ	k	M	p_c (MPa)
1	Linear-elastic	100	0.25	–	–	–	–	–	–
2	Elastic–plastic	1,000	0.30	30	1.00	–	–	–	–
3	Modified Cam-Clay	–	0.25	–	–	2.00	0.003	1.50	6.00

E Young's modulus, v Poisson's ratio, ϕ shear angle, c cohesion, λ logarithmic hardening constant for plastic response in pure compression, k logarithmic bulk modulus, p_c initial size of yield surface

pillars for which the size may progressively vary, and the estimation of the in situ (initial, after excavation) conditions.

Pillar failure conditions were analysed through the increase of vertical loads, from imposing vertical displacements (δv_{gs}) acting on the ground surface (g.s.). Although real pillars are loaded by a force, this displacement controlled loading technique was preferred for load control to explore the pillar behaviour in both pre- and post-peak strength phases. This second phase must not be neglected because collapsed pillars (beyond the peak value) actually continue to bear a non-negligible portion of the external loads, influencing the load transfer to adjoining pillars. Note that the displacement controlled loading technique does not sensibly influences the simulated global response of the pillar and the maximum "equivalent" overcharge that the system can sustain (i.e. pillar collapse condition).

The structural responses of 67 pillar models that differed in the shape of the horizontal cross-section (square, circular, rectangular) and the height were numerically simulated (see Table 3). Further analyses were carried out to evaluate the influence of the mechanical parameters of the pillar-constituent material on the mechanical response as a whole.

4 Numerical Results

The prescribed displacements of the ground surface shortened the height of the pillar and widened its cross-sectional area (orthogonal to the pillar axis). However, because of the roof stiffness, the pillar was not uniformly loaded; thus, during the excavation phases, non-uniform stresses and strains occurred both in the roof and pillar. The reduced confinement allowed the maximum strains to affect the external regions of the pillar. At the roof-pillar and base-pillar connections, the shear stresses further increased the local material confinement and prevented transversal dilatations, for which the maximum values were observed at the pillar mid-height. Because of the non-homogeneous confinement, material yielding first occurred in the more stressed pillar regions and then developed throughout the whole pillar. The stress distribution in the pillar evolved according to the progressive material yielding. Because of this complex behaviour, the global pillar response cannot be described solely on the basis of local information; instead, representative global variables have to be defined and examined.

4.1 Global Response Variables

The pillar loading state is represented by the average vertical stress σ_p acting on a horizontal cross-section at the mid-height of the pillar:

$$\sigma_p = \sigma_p(\delta v_{gs}) = \sigma_p^{\gamma} + \Delta\sigma_p(\delta v_{gs}) \tag{7}$$

where σ_p^{γ} is the mean vertical stress deriving from the weight of coating soils (tributary area) and $\Delta\sigma_p$ is the average stress increment due to external loads variations (i.e. imposed δv_{gs}).

The deformation state is characterised through the pillar average axial strain:

$$\varepsilon_p = \varepsilon_p(\delta v_{gs}) = \frac{\Delta h}{h_i} = \frac{h_i - h(\delta v_{gs})}{h_i} \tag{8}$$

where h_i represents the pillar height after excavation and Δh denotes its shortening (computed along its symmetry axis).

Strains occurring with excavation are referred to the reference undeformed configuration of the pillar ($\varepsilon_p = 0$), while associated stresses ($\sigma_p^{\gamma} \neq 0$) are considered in the successive steps of the analysis.

The $(\sigma_p, \varepsilon_p)$ curve represents the constitutive relationship of the whole pillar, which is considered as a macro-element loaded vertically. Note that the mechanical properties of the upper soil layers affect the response of the whole geotechnical system. In turn, this may attain a global ultimate limit state due to a possible failure of different structural elements (e.g. the roofs); however, the variation in the upper soils does not affect the $(\sigma_p, \varepsilon_p)$ response of a single pillar nor its failure state.

4.2 Influence of Pillar Cross-Section Area

The influence of the area A of the pillar cross-section on the pillar strength σ_r was examined through the simulation of several virtual load tests on square-shaped pillars.

Table 3 Geometrical properties of analysed pillars

Id.	Shape	b (m)	l (m)	d (m)	b_{eq} (m)	h (m)	$\frac{b}{l}$	$\frac{b}{h}$	A (m^2)
1	C	–	–	9,00	7.98	3.50	–	–	63.62
2	C	–	–	8.00	7.09	3.50	–	–	50.27
3	C	–	–	7.00	6.20	3.50	–	–	38.48
4	C	–	–	6.00	5.32	3.50	–	–	28.27
5	C	–	–	5.00	4.43	3.50	–	–	19.63
6	C	–	–	4.00	3.54	3.50	–	–	12.57
7	C	–	–	3.00	2.66	3.50	–	–	7.07
8	S	7.98	7.98	–	7.98	3.50–4.50–5.50	1.00	2.28	63.62
9	S	7.09	7.09	–	7.09	3.50–4.50–5.50	1.00	2.03	50.27
10	S	6.20	6.20	–	6.20	3.50–4.50–5.50	1.00	1.77	38.48
11	S	5.32	5.32	–	5.32	3.50–4.50–5.50	1.00	1.52	28.27
12	S	4.43	4.43	–	4.43	3.50–4.50–5.50	1.00	1.27	19.63
13	S	3.54	3.54	–	3.54	3.50–4.50–5.50	1.00	1.01	12.57
14	S	2.66	2.66	–	2.66	3.50–4.50–5.50	1.00	0.76	7.07
15	R	7.08	7.97	–	7.51	3.50	0.89	2.02	56.43
16	R	6.2	7.97	–	7.03	3.50	0.78	1.77	49.41
17	R	5.31	7.97	–	6.51	3.50	0.67	1.52	42.32
18	R	4.43	7.97	–	5.94	3.50	0.56	1.27	35.31
19	R	3.54	7.97	–	5.31	3.50	0.44	1.01	28.21
20	R	2.65	7.97	–	4.60	3.50	0.33	0.76	21.12
21	R	1.77	7.97	–	3.76	3.50	0.22	0.51	14.11
22	R	6.2	7.08	–	6.63	3.50	0.88	1.77	43.90
23	R	5.31	7.08	–	6.13	3.50	0.75	1.52	37.59
24	R	4.42	7.08	–	5.59	3.50	0.62	1.26	31.29
25	R	3.54	7.08	–	5.01	3.50	0.50	1.01	25.06
26	R	2.65	7.08	–	4.33	3.50	0.37	0.76	18.76
27	R	1.76	7.08	–	3.53	3.50	0.25	0.50	12.46
28	R	5.31	6.2	–	5.74	3.50	0.86	1.52	32.92
29	R	4.43	6.2	–	5.24	3.50	0.71	1.27	27.47
30	R	3.54	6.2	–	4.68	3.50	0.57	1.01	21.95
31	R	2.66	6.2	–	4.06	3.50	0.43	0.76	16.49
32	R	1.77	6.2	–	3.31	3.50	0.29	0.51	10.97
33	R	4.43	5.31	–	4.85	3.50	0.83	1.27	23.52
34	R	3.54	5.31	–	4.34	3.50	0.67	1.01	18.80
35	R	2.65	5.31	–	3.75	3.50	0.50	0.76	14.07
36	R	1.77	5.31	–	3.07	3.50	0.33	0.51	9.40
37	R	3.54	4.43	–	3.96	3.50	0.80	1.01	15.68
38	R	2.66	4.43	–	3.43	3.50	0.60	0.76	11.78
39	R	1.77	4.43	–	2.80	3.50	0.40	0.51	7.84
40	R	2.65	3.54	–	3.06	3.50	0.75	0.76	9.38
41	R	1.77	3.54	–	2.50	3.50	0.50	0.51	6.27
42	R	6.91	9.21	–	7.98	3.50	0.75	1.97	63.64
43	R	6.14	8.19	–	7.09	3.50	0.75	1.75	50.29
44	R	5.37	7.16	–	6.20	3.50	0.75	1.53	38.45
45	R	4.6	6.14	–	5.31	3.50	0.75	1.31	28.24
46	R	3.84	5.12	–	4.43	3.50	0.75	1.10	19.66
47	R	3.07	4.09	–	3.54	3.50	0.75	0.88	12.56
48	R	2.3	3.07	–	2.66	3.50	0.75	0.66	7.06

Table 3 continued

Id.	Shape	b (m)	l (m)	d (m)	b_{eq} (m)	h (m)	$\frac{b}{l}$	$\frac{b}{h}$	A (m^2)
49	R	5.64	11.28	–	7.98	3.50	0.50	1.61	63.62
50	R	5.01	10.03	–	7.09	3.50	0.50	1.43	50.25
51	R	4.39	8.77	–	6.20	3.50	0.50	1.25	38.50
52	R	3.76	7.52	–	5.32	3.50	0.50	1.07	28.28
53	R	3.13	6.27	–	4.43	3.50	0.50	0.89	19.63
54	R	2.51	5.01	–	3.55	3.50	0.50	0.72	12.58
55	R	1.88	3.76	–	2.66	3.50	0.50	0.54	7.07

b small side of cross-section, l large side of cross-section, d cross-section diameter (for cylindrical pillars), A cross-section area, h height, $b_{\mathrm{eq}} = \sqrt{A}$ side of equivalent square section pillar; shape of cross-section: C = circular, S = square, R = rectangular

Figure 3 shows the global responses of square pillars with an area A ranging between 7.1 and 63.6 m^2. For these pillars ($h = 3.5$ m), the width-to-height ratios b/h varied in the range between 0.8 and 2.3.

The average pillar stress σ_{p} non-linearly increased from the initial value $\sigma_{\mathrm{p}}^{\gamma}$ up to the yielding stress σ_{p}^{y}. The only exception was the smallest pillar ($A = 7.1\,\mathrm{m}^2$), which was strongly affected by plastic strains that arose during the excavation phase. The yielding condition was identified by the stress–strain state $(\sigma_{\mathrm{p}}^{y}, \varepsilon_{\mathrm{p}}^{y})$ at which the pseudo-linear trend ends and the slope of the curve $(\sigma_{\mathrm{p}}, \varepsilon_{\mathrm{p}})$ changes. In conventional analytical methods, σ_{p}^{y} represents the ultimate pillar strength σ_{r}. The most slender pillars (small A values, ≤ 20 m^2) exhibited a peak strength σ_{p}^{y} coupled with a brittle post-peak behaviour. For larger pillars, ductile behaviours were observed. In this case, because of the displacement controlled loading technique, σ_{p}^{y} did not correspond to the maximum stress on the $(\sigma_{\mathrm{p}}, \varepsilon_{\mathrm{p}})$ plane.

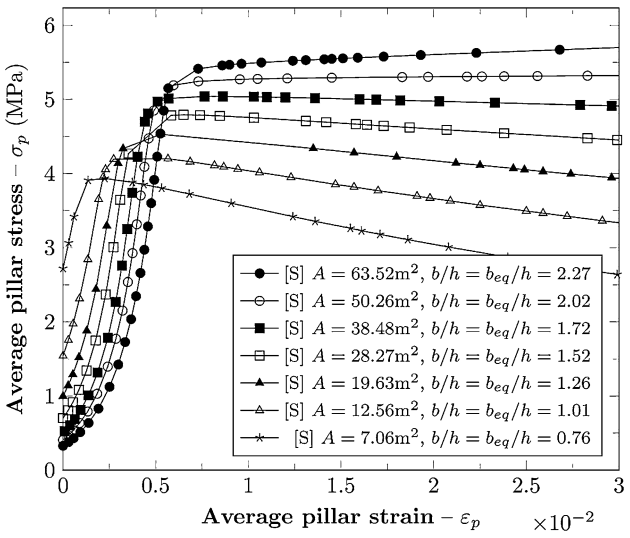

Fig. 3 Global responses of square section pillars with constant height ($h = 3.5$ m) and cross-section area of 7.1–63.6 m^2

Based on a vertical section along the diagonal of a representative pillar ($A = 28.3\,\mathrm{m}^2$, $h = 3.5\,\mathrm{m}$, $b/h = 1.5$), Fig. 4 depicts the vector representation of principal stresses and the associated evolution of plastic strains corresponding to the six phases through which the test developed.

The stress distribution inside the pillar evolved according to the progressive local yielding. After excavation ($\delta v_{\mathrm{gs}} = 0$), the greatest stresses occurred at the corners of the base-pillar and roof-pillar connections. The internal regions, close to the symmetry axis of the pillar, bore small stresses. High shear stresses at the roof-pillar and pillar-base connections induced appreciable rotations, with respect to the external reference system, of the principal stresses. The rotations progressively decreased (for the whole pillar height) in proximity to the symmetry axis, along which the maximum principal stresses coincided with the vertical ones. In this phase, referring to the horizontal cross-section at the mid-height of the pillar, the greatest principal stress approximately coincided with the vertical stress for each volume element.

The progressive increase in the imposed vertical g.s. displacements δv_{gs} initially induced an increase in stresses of the most stressed elements (upper and lower corners), until yielding. Stress redistribution then took place: new plastic strains developed first affecting large sub-horizontal volumes of materials near the base of the pillar and the roof-pillar connection. Then, the plastic strains affected the external parts of the mid-height pillar; at the peak-strength condition, this section fully yielded; additional displacements δv_{gs} further increased the plastic strains in the internal parts of the pillar. During this final phase, most of the applied load was borne by the internal and better confined volumes of the pillar. Principal stresses within the pillars tended to align according to a *hourglass*-shaped configuration.

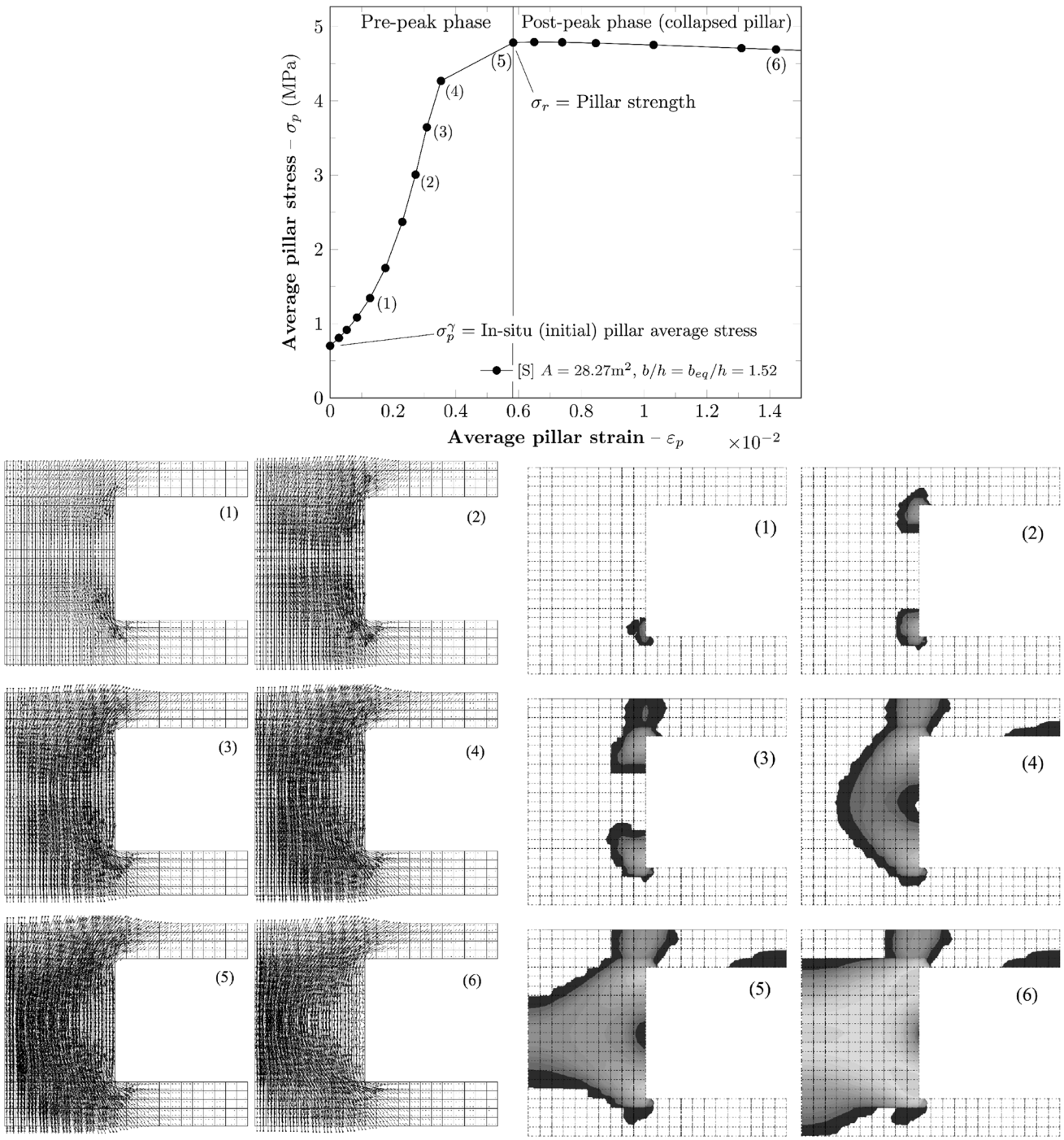

Fig. 4 Evolution of principal stresses and yielding in a vertical section crossing the diagonal of a representative squared pillar (six phases of the *virtual* load test). The yielding process is represented through the plastic strain magnitude $\varepsilon^{\text{pl}}_{\text{mag}} = \sqrt{2\,\varepsilon^{\text{pl}}_{ij} : \varepsilon^{\text{pl}}_{ij}/3}$, where $\varepsilon^{\text{pl}}_{ij}$ is the plastic strains tensor

The numerical results, particularly the plastic strain evolution in the pillar, appreciably agreed with the experimental observations of Martinetti and Ribacchi (1964). In particular, the simulation results and in situ observations showed a strong fitness for phases close to the conventional pillar collapse. Under this condition, the external and less confined parts of the pillar became highly plasticized and bore very small loads. The peculiar *hourglass*-shaped configuration assumed by the principal stress distribution may be related to the similar observations of highly damaged pillars.

4.3 Influence of Pillar Geometry: Shape and Height

Circular (2D axi-symmetric analyses) and rectangular pillars were analysed to examine the role of the cross-sectional shape on the pillar's mechanical response. The rectangular pillars were first obtained from square pillars by reducing one side width (b) and keeping the other one unchanged ($l > b$). This procedure allowed the same FE mesh used for the square pillars to be maintained for an objective evaluation (i.e. absence of possible approximations deriving from mesh differences) of the combined effects of A, b and l on the pillar strength. The stability conditions of rectangular pillars were then investigated for different cross-section ratios b/l. This approach allowed the parameter A to be fixed and isolated the influence of the pillar shape.

Figure 5a compares the simulated responses of circular and square pillars. Figure 5b compares the responses of rectangular and square pillars. In both cases, the pillar responses were compared to homogeneous groups in terms of the cross-sectional area A and height ($h = 3.5$ m).

The numerical results showed that the pillar response was not significantly influenced by the shape of the pillar cross-section, but mainly depended on the area A. For a given value of A, the global responses $(\sigma_p, \varepsilon_p)$ were analogous over the whole range of the simulated pillar deformations ε_p. This was true even for the circular pillars, although the axi-symmetric modelling assumption introduced strong simplifications both from the geometrical and mechanical points of view.

The height h was also found to significantly influence the pillar mechanical response. This was examined through the simulation of square pillars with h variable in the range between 3.5 and 5.5 m. For a given cross-section area A, the taller pillars showed a less stiff pseudo-elastic response and a more pronounced brittleness in post-peak phase (Fig. 5c). In some cases, this led to a transition from ductile to brittle behaviour. As expected, a taller pillar generally led to a lower ultimate resistance σ_r.

Figure 6a plots the strength values obtained from the above virtual load tests against the pillar width-to-height ratio b/h. Although σ_r increased with b/h, the numerical results demonstrated an appreciable dispersion (correlation coefficient $R^2 = 0.70$). Therefore, the standard (original) analytical formulations could not be applied to the present case. Based on the obtained results, however, their formal validity can be restored if one observes that the *average width-to-height ratio*:

$$\frac{b_{eq}}{h} = \frac{\sqrt{A}}{h} \tag{9}$$

is a proper geometric parameter to represent the evolution of σ_r. In other words, rectangular pillars can be

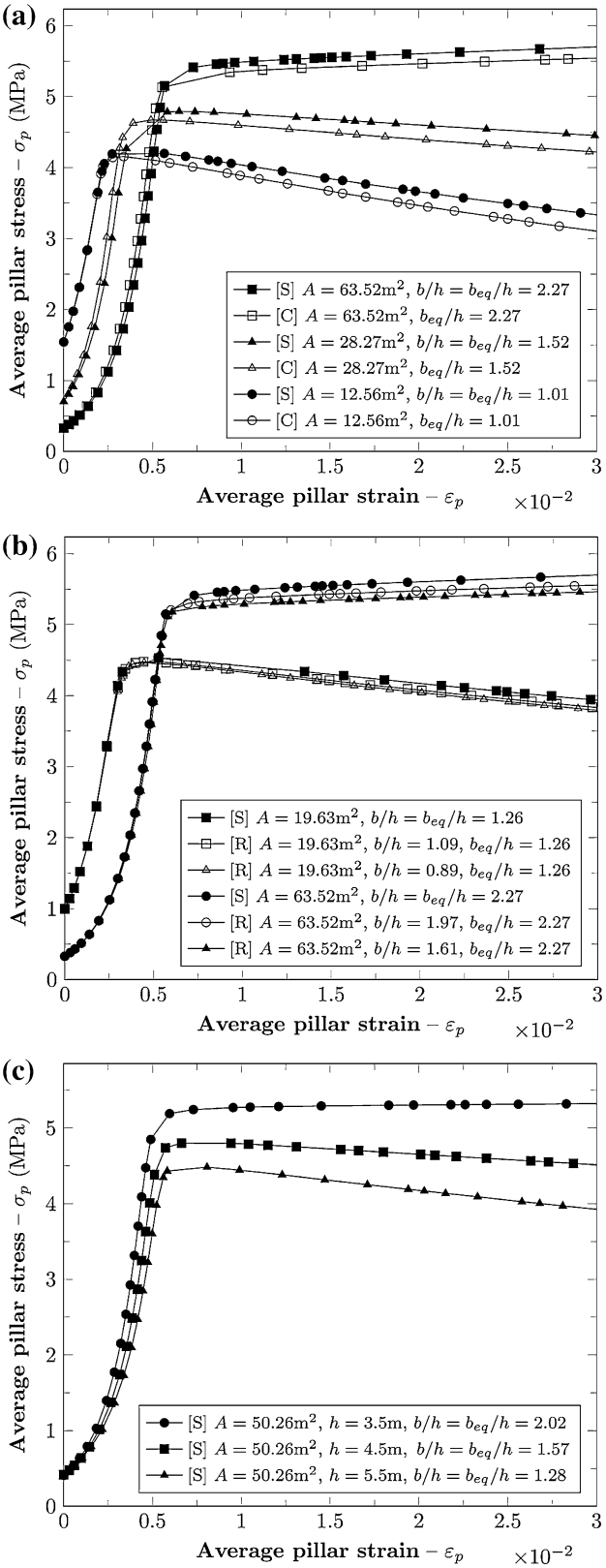

Fig. 5 Comparison of global responses: **a** three couples of square and cylindrical (axi-symmetric) pillars; **b** two triplets of square and rectangular pillars having the same cross-section area and ratio of the sides $b/l = 0.5$ and 0.75; **c** three pillars having equal area and height h variable in the range between 3.5 and 5.5 m

schematised as equivalent square section pillars with sides $b_{eq} = \sqrt{A}$ in length. Once this variable is applied, a linear regression characterised by a high correlation coefficient ($R^2 \geq 0.97$) can represent, as a whole, the numerically computed strength values for all simulated (circular, square and rectangular) pillars (Fig. 6b):

$$\sigma_r = \alpha_1 + \alpha_2 \frac{b_{eq}}{h} \tag{10}$$

Parameters α_1 and α_2 in Eq. (10) assume constant values in computations: $\alpha_1 = 0.99$ and $\alpha_2 = 3.17$. However, they depend on the mechanical properties of the pillar material, specifically the preconsolidation pressure p_c and slope of the critical state line M on the (q, p) plane:

$$\alpha_1 = \alpha_1(p_c, M), \quad \alpha_2 = \alpha_2(p_c, M). \tag{11}$$

4.4 Influence of Mechanical Parameters of Pillar Material

The role of the mechanical parameters of soft rock was investigated by simulating virtual load tests (further 144 simulations) on square cross-section pillars with a variable h. According to previous results, the influence of the shape of the pillar cross-section was neglected.

The preconsolidation pressure p_c and slope of the critical state M varied for nine combinations (Table 4). The remaining parameters (λ, k and ν) required to define the modified Cam-Clay model were kept constant, as their variability has been observed to be limited in experiments (Cecconi 1999). Conversely, many authors (Cecconi et al. 2002; Nova et al. 2003) have shown that the size of the yield locus and the critical state conditions may significantly vary according to mechanical (e.g. grain crushing and debonding) and non-mechanical (e.g. chemical weathering) material degradation.

Figure 7 shows the global responses of representative pillars. Numerical analyses showed that the pillar response was appreciably influenced by p_c and M over the whole range of simulated deformations ε_p. In particular, variations in p_c mainly induced variations in the pillar strength but did not directly influence the post-peak behaviour (Fig. 7a). When p_c was kept constant, a change in M changed both the resistance of the pillar and the post-peak behaviour (Fig. 7b). The pillar brittleness gradually decreased with increasing M; for slender pillars (i.e. lower average width-to-height b_{eq}/h ratios), a transition from ductile to brittle behaviour sometimes occurred.

As shown in Fig. 8, when b_{eq}/h and M were fixed, the relationship between the pillar compressive strength and the preconsolidation pressure was approximately linear. A simple linear regression model without the intercept term fits the numerical results:

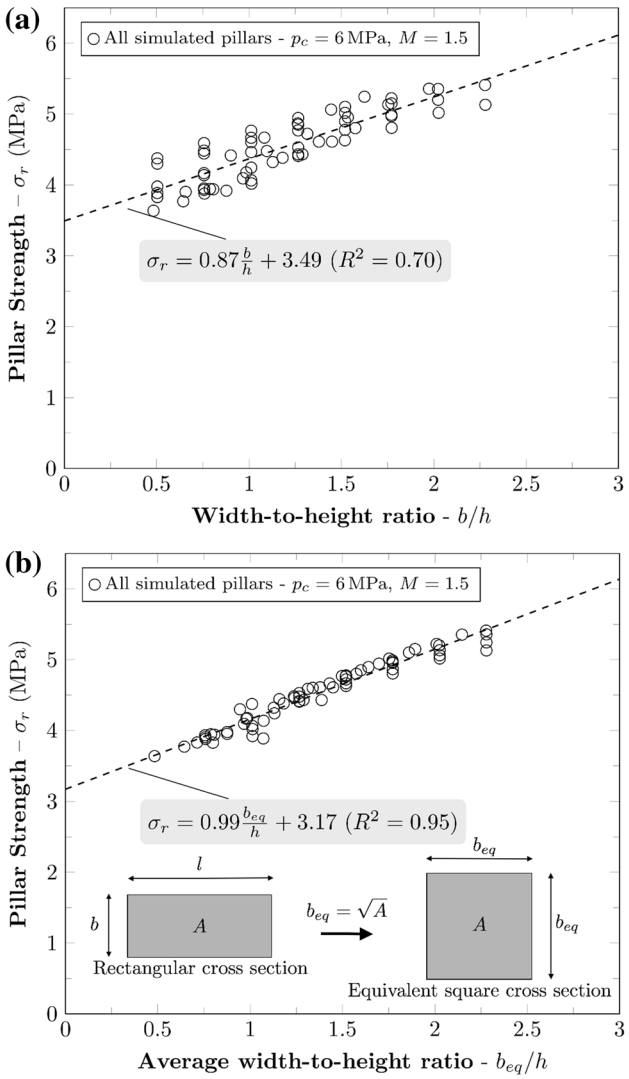

Fig. 6 Numerically computed pillar strength values σ_r (for square, circular and rectangular pillars and different pillar heights h) against width-to-height b/h and average width-to-height b_{eq}/h ratios

Table 4 Mechanical parameters assigned to pillar material for analysis of their influence on the pillar behaviour

Id. Mat.	λ	k	ν	M	p_c (MPa)
MCC1	0.13	0.0032	0.25	1.20	3.00
MCC2	0.13	0.0032	0.25	1.30	3.00
MCC3	0.13	0.0032	0.25	1.50	3.00
MCC4	0.13	0.0032	0.25	1.20	4.50
MCC5	0.13	0.0032	0.25	1.30	4.50
MCC6	0.13	0.0032	0.25	1.50	4.50
MCC7	0.13	0.0032	0.25	1.20	6.00
MCC8	0.13	0.0032	0.25	1.30	6.00
MCC9	0.13	0.0032	0.25	1.50	6.00

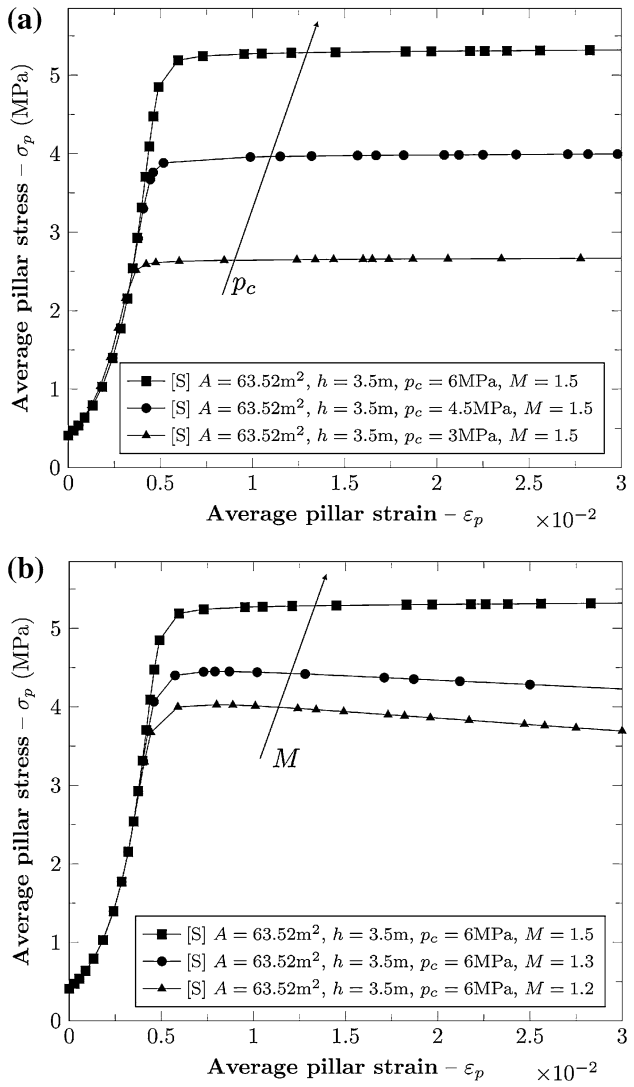

Fig. 7 Influence of p_c and M on the global response of a representative square pillar ($A = 63.52\,\text{m}^2$, $h = 3.5\,\text{m}$): **a** p_c is variable and M is fixed; **b** p_c is fixed and M is variable

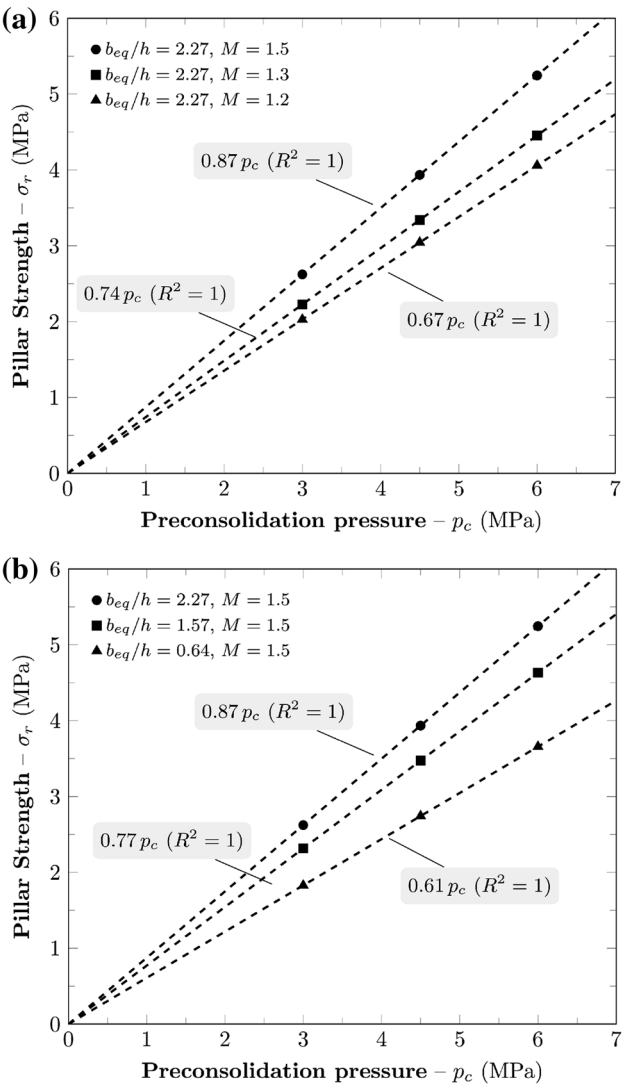

Fig. 8 Evolution of σ_r with respect to preconsolidation pressure p_c: **a** for fixed value of average width-to-height ratio b_{eq}/h and three values of M; **b** for fixed M and three values of b_{eq}/h

$$\sigma_r = \alpha_3(M, b_{eq}/h)p_c. \tag{12}$$

The angular coefficient α_3 increased with M (i.e. material shear resistance) and b_{eq}/h (i.e. area of the cross-section). This dependency can be better explained by plotting the ratio σ_r/p_c against M for different values of b_{eq}/h (Fig. 9). This representation easily shows the family of linear regressions:

$$\begin{aligned}\sigma_r/p_c &= \alpha_3(M, b_{eq}/h) \\ &= \alpha_4(b_{eq}/h) + \alpha_5 M,\end{aligned} \tag{13}$$

where $\alpha_5 = 0.66$ provided the best fit for the data points. As shown in Fig. 9, the intercept $\alpha_4(b_{eq}/h)$ was almost independent of the parameter M, while it monotonically increased with b_{eq}/h.

The next section provides functional forms allowing a proper representation of the pillar strength evolution according to the three considered parameters (b_{eq}/h, M and p_c).

5 Novel Pillar Strength Formula

As shown in Fig. 10, the results presented in the previous sections demonstrate the following linear regression:

$$\sigma_r = \alpha_1(p_c, M) + \alpha_2(p_c, M)\frac{b_{eq}}{h} \tag{14}$$

which fits with high correlation coefficients ($R^2 \geq 0.97$) the computed strength values σ_r for all simulated pillars.

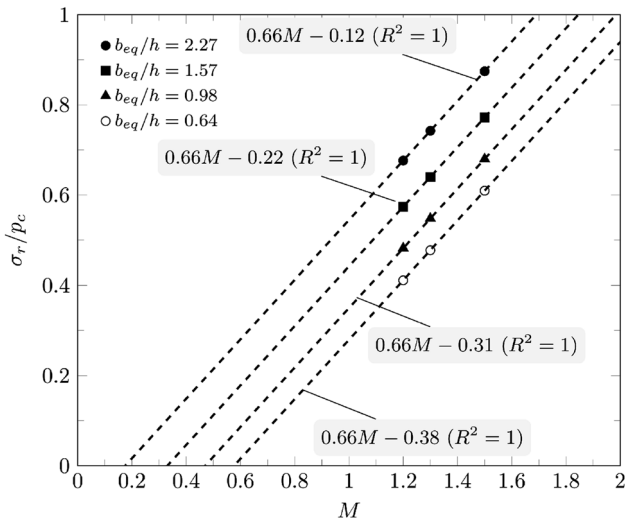

Fig. 9 Pillar strength to preconsolidation pressure σ_r/p_c ratio plotted against M for four values of average width-to-height ratio b_{eq}/h

The numerical results can be easily reworked to clarify the relations $\alpha_1(p_c, M)$ and $\alpha_2(p_c, M)$ in Eq. (14). In particular, the linear regressions proposed in Fig. 10 directly show that the slopes of the $(\sigma_r, b_{eq}/h)$ curves are quite independent of the parameter M, while a very simple linear regression approximates $(R^2 = 0.98)$ their dependency on p_c:

$$\alpha_1(p_c) = 0.17\, p_c \tag{15}$$

Furthermore, $\alpha_2(p_c, M)$ can be easily expressed as:

$$\alpha_2(p_c, M) = (0.62\, M - 0.41) p_c. \tag{16}$$

Substituting Eqs. (15) and (16) into Eq. (14) obtains the following relationship:

$$\sigma_r = p_c \left[0.62\, M - 0.41 + 0.17\, \frac{b_{eq}}{h} \right], \tag{17}$$

where σ_r and p_c are expressed in MPa. Note that by relying σ_r to the preconsolidation pressure instead of the uniaxial strength, as in conventional analytical formulations, the pillar strength is implicitly related to the material resistance along all of the spatial directions. Furthermore, the material shear resistance is directly considered through the slope of the critical state line M, which in turn is related to the shear resistance angle ϕ.

Figure 11 compares the predictions of the proposed original formulation and three well-known conventional empirical formulas (Salamon and Munro 1967; Obert and Duvall 1967; Lunder and Pakalnis 1997). For the sake of simplicity, only square section pillars were considered. Figure 11a shows the results when $b = b_{eq}$ was varied and the pillar height h was fixed at 4 m, while Fig. 11b shows

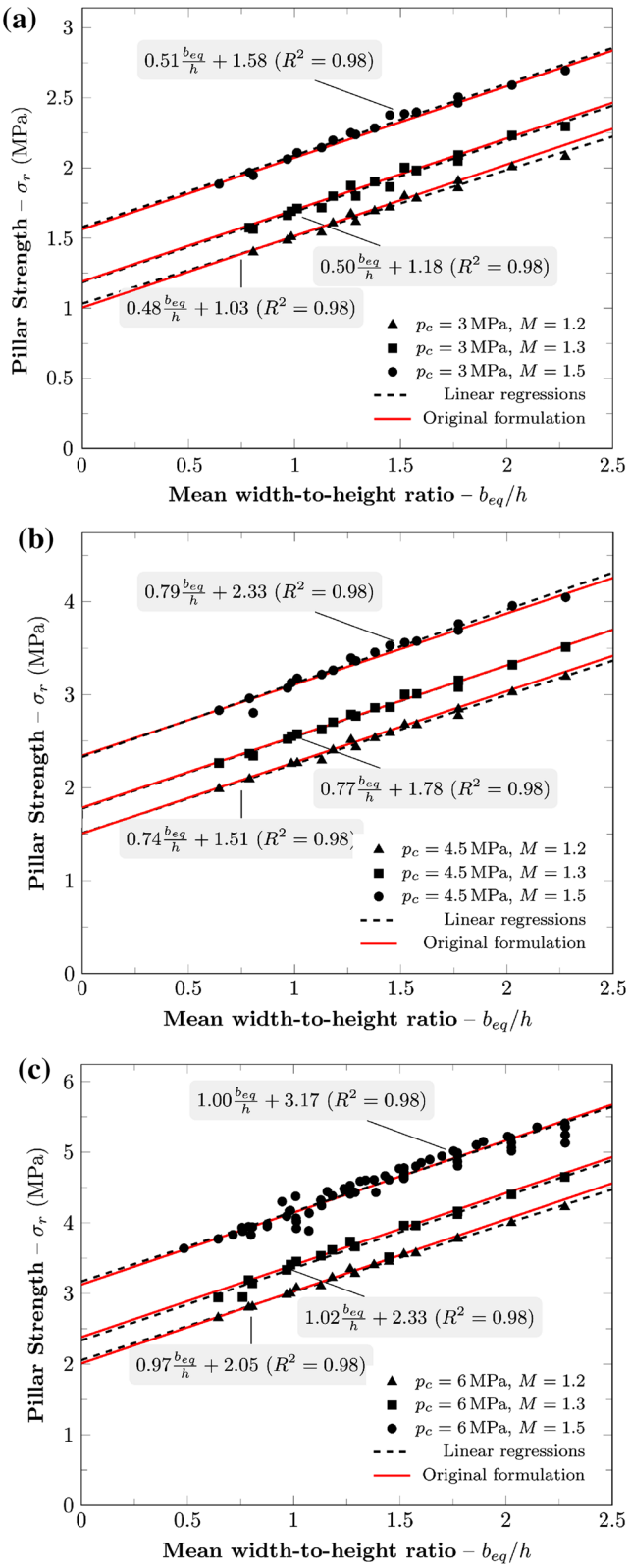

Fig. 10 Pillar strength evolution in function of average pillar width-to-height ratio and comparison with values predicted by the proposed original formulation (17)

the results when b was fixed at 6 m and h was varied. The mechanical parameters of the pillar material were assigned according to typical values for Roman pozzolana (Cecconi 1999) (uniaxial compressive strength: $\sigma_1 = 2\,\text{MPa}$; unconfined compressive strength: $\sigma_u = 1.9\,\text{MPa}$; $p_c = 3\,\text{MPa}$ and $M = 1.4$).

For typical geometries of the pillars in the Roman area, the formulas predicted similar strength values σ_r. However, the proposed expression (17) was less conservative than the traditional ones for all pillars. This was partly because the conventional pillar strength formulas neglect the effect of the confining stress and relate the pillar strength only to the uniaxial compressive strength σ_1. The only exception is the formula presented by Lunder and Pakalnis (1997), which accounts for the confinement effect through the parameter k_lp defined in Table 1.

The role of the confining stress should become significant for larger pillars, dealing to higher strength values. However, as shown in Fig. 11, the Lunder and Pakalnis's formulation predicted lower strength values for all the considered pillar dimensions.

Note that these comparisons only provide qualitative information because the values of the parameters figuring in the conventional formulas were derived from the analysis of hard rock mines. Therefore, their application to other mines and materials (e.g. soft rocks) require proper parameter identification, based on in situ observations of failed/stable pillars.

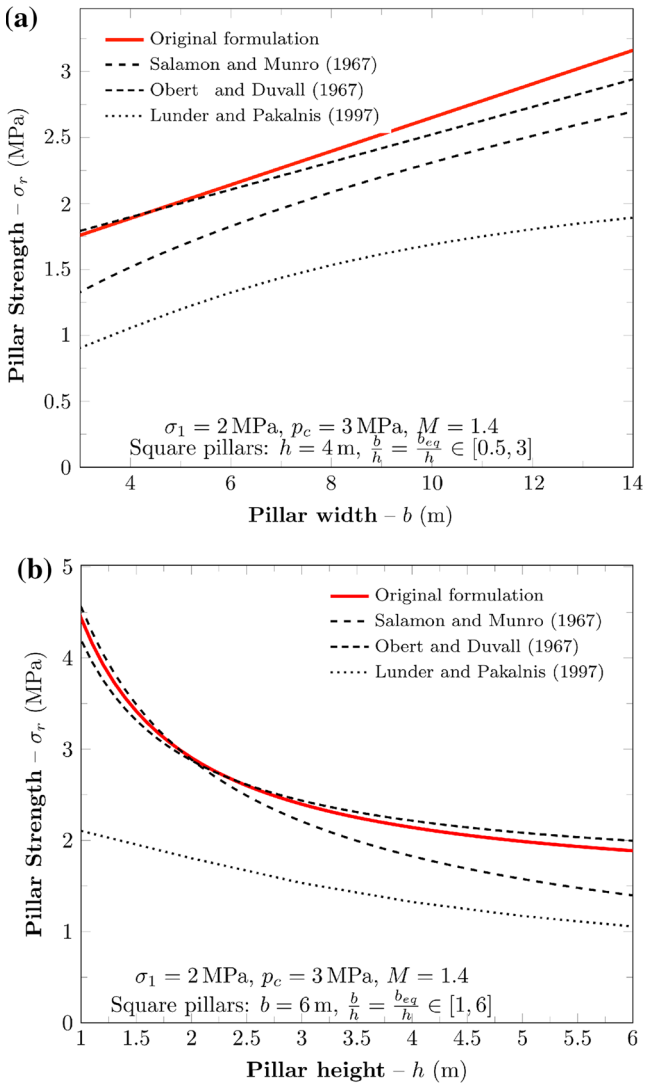

Fig. 11 Comparison of pillar strengths from proposed original formulation and three well-known formulations: **a** $h = 4\,\text{m}$ is fixed and b varies in the range between 3 and 14 m; **b** $b = 6\,\text{m}$ is fixed and h ranges between 1 and 6 m

6 Concluding Remarks

The global stress–strain behaviour of soft rock pillars in systems of shallow cavities, under vertical loads, was numerically simulated through FEA. The features of the soft rock were simulated with a Modified Cam-Clay model to represent the transition from brittle-dilatant to ductile-contractant behaviour with increasing preconsolidation pressure. The effects of the pillar geometry (cross-section area, shape, height, slenderness) and the mechanical parameters characterising the constitutive model were numerically evaluated.

The results showed that the pillar strength σ_r mainly depends on the area A of the pillar horizontal cross-section, the height h, and the mechanical properties of the constituent material. The shape of the cross-section does not play an appreciable role on the pillar strength, despite what is commonly stated by conventional analytical formulations.

Based on the results, a geometrical parameter which describes the influence of the pillar geometry on its compressive resistance is the average width-to-height ratio b_eq/h, where $b_\text{eq} = \sqrt{A}$. With regard to the mechanical parameters of soft rocks, σ_r was observed to be strongly dependent on the preconsolidation pressure p_c and slope M of the critical state line on the (p, q) plane.

Finally, a novel formula that directly relates σ_r to the pillar geometry and the mechanical parameters of the composing materials (p_c, M) was developed. In this formulation, the pillar strength directly relies on the preconsolidation pressure, instead of the uniaxial strength as in conventional analytical formulas. This allows the increase in σ_r due to the material resistance along all spatial directions to be considered implicitly. The material shear resistance is also considered, as the slope of the critical state line M can be related to the friction angle ϕ (e.g. in triaxial compression conditions, $M = 6\,\sin\phi/(3 - \sin\phi)$).

Further research efforts are still needed to experimentally validate the proposed formulation and analyse its dependency on the constitutive model representing the mechanical behaviour of the soft rock.

References

Airey D (1993) Triaxial testing of naturally cemented carbonate soil. J Geotech Eng 119:1379–1398

Aversa S, Evangelista A (1998) The mechanical behaviour of a pyroclastic rock: yield strength and "destructuration effects". Rock Mech Rock Eng 31(1):25–42

Bieniawski Z (1984) Rock mechanics design in mining and tunneling. AA Balkema, Rotterdam

Brady B, Brown E (2004) Rock mechanics, for underground mining. Kluwer Academic Publishers, Dordrecht

Cecconi M (1999) Structural characteristics and mechanical properties of a pyroclastic rock. PhD thesis, Dept. of Civil Engineering, University of Rome Tor Vergata (in italian)

Cecconi M, De Simone A, Tamagnini C, Viggiani G (2002) A constitutive model for granular materials with grain crushing and its application to a pyroclastic soil. Int J Numer Anal Methods Geomech 26(15):1531–1560

Coop M, Atkinson J (1993) The mechanics of cemented carbonate sands. Geotechnique 43(1):53–67

DeSimone A, Tamagnini C (2005) Stress–dilatancy based modelling of granular materials and extensions to soils with crushable grains. Int J Numer Anal Methods Geomech 29(1):73–101

Elliott G, Brown E (1985) Yield of a soft, high porosity rock. Geotechnique 35(4):413–423

Federico F, Screpanti S (2002) Stability analysis of cavities excavated in roman pyroclastic rocks. In: XXI Convegno Nazionale di Geotecnica Opere geotecniche in ambiente urbano, L'aquila (in italian)

Federico F, Screpanti S (2003a) Analytical criteria and numerical procedures for safety analyses of pillars and vaults excavated in pyroclastic rocks. In: XXII Convegno Nazionale di Geotecnica, Palermo (in italian)

Federico F, Screpanti S (2003b) Effects of filling shallow room and pillar mines in weak pyroclastic rock. In: XIIIth European conference on soil mechanics and geotechnical engineering: geotechnical problems with man-made and man influenced grounds

Federico F, Screpanti S, Rastiello G (2010) Stress–strain behaviour of a soft-rock pillar acted upon vertical loads. In: Benz T, Nordal S (eds) NUMGE 2010-European conference on numerical methods in geotechnical engineering. CRC Press, Boca Raton

González-Nicieza C, Álvarez-Fernández M, Menéndez-Díaz A, Álvarez-Vigil A (2006) A comparative analysis of pillar design methods and its application to marble mines. Rock Mech Rock Eng 39(5):421–444

Griffiths D, Fenton G, Lemons C (2002) Probabilistic analysis of underground pillar stability. Int J Numer Anal Methods Geomech 26(8):775–791

Hedley D, Grant F (1972) Stope-and-pillar design for the Elliot Lake Uranium Mines. Can Inst Min Metall Bull 65(723):37–44

Jaiswal A, Shrivastva B (2009) Numerical simulation of coal pillar strength. Int J Rock Mech Min Sci 46(4):779–788. doi:10.1016/j.ijrmms.2008.11.003

Lagioia R, Nova R (1996) An experimental and theoretical study of the behaviour of a calcarenite in triaxial compression. Int J Rock Mech Min Sci Geomech Abstr 33(5):202A–203A

Leroueil S, Vaughan P (1990) General and congruent effects of structure in natural soils and weak rocks. Geotechnique 40: 467–88

Lunder P, Pakalnis R (1997) Determination of the strength of hard-rock mine pillars. CIM Bull 90(1013):51–55

Maccarini M (1987) Laboratory studies of a weakly bonded artificial soil. PhD thesis, University of London

Martin C, Maybee W (2000) The strength of hard-rock pillars. Int J Rock Mech Min Sci 37(8):1239–1246

Martinetti S, Ribacchi R (1964) Osservazioni sul comportamento statico dei pilastri di una cava in sotterraneo di materiali piroclastici. In: Simp. Probl. Geomin. Sardi, Cagliari

Mortazavi A, Hassani F, Shabani M (2009) A numerical investigation of rock pillar failure mechanism in underground openings. Comput Geotech 36(5):691–697. doi:10.1016/j.compgeo.2008.11.004

Murali Mohan G, Sheorey P, Kushwaha A (2001) Numerical estimation of pillar strength in coal mines. Int J Rock Mech Min Sci 38(8):1185–1192

Navarro V, Candel M, Barenca A, Yustres A, Garcia B (2007) Optimisation procedure for choosing cam clay parameters. Comput Geotech 34(6):524–531

Nova R, Wood D (1979) A constitutive model for sand in triaxial compression. Int J Numer Anal Methods Geomech 3:255–278

Nova R, Castellanza R, Tamagnini C (2003) A constitutive model for bonded geomaterials subject to mechanical and/or chemical degradation. Int J Numer Anal Methods Geomech 27(9): 705–732

Obert L, Duvall W (1967) Rock mechanics and the design of structures in rock. Wiley, New York

Qin S, Jiao J, Tang C, Li Z (2006) Instability leading to coal bumps and nonlinear evolutionary mechanisms for a coal-pillar-and-roof system. Int J Solids Struct 43(25–26):7407–7423

Roscoe K, Burland J (1968) On the generalized stress–strain behaviour of wet clay. Eng Plasticity 48:535–609

Rouainia M et al (2000) A kinematic hardening constitutive model for natural clays with loss of structure. Geotechnique 50(2):153–164

Rowe PW (1962) The stress–dilatancy relation for static equilibrium of an assembly of particles in contact. Proc R Soc Lond Ser A Math Phys Sci 269(1339):500–527

Salamon M, Munro A (1967) A study of strength of coal pillars. J South Afr Inst Min Metallurgy 68(2):55

Schofield A, Wroth C (1968) Critical state soil mechanics. Mc Graw Hill, London

Simulia (2009) ABAQUS manual. Dassault Systems

Von Kimmelmann M, Hyde B, Madgwick R (1984) The use of computer applications at bcl limited in planning pillar extraction and design of mining layouts. Proceedings of ISRM symposium: design and performance of underground excavations. British Geotechnical Society, London, pp 53–63

Wang S, Lam K, Au S, Tang C, Zhu W, Yang T (2006) Analytical and numerical study on the pillar rockbursts mechanism. Rock Mech Rock Eng 39(5):445–467

Wood DM, Mackenzie N, Chan A (1992) Selection of parameters for numerical predictions. Predictive soil mechanics: proceedings of the wroth memorial symposium, Oxford. UK. Thomas Telford, London, pp 496–512